UNVEILING BIOLOGICAL PRINCIPLES THROUGH BIOBOTS

ROBERTA SANTORIELLO[*], FRANCESCO VIOLA[†] AND VINCENZO CITRO[*]

[*]Department of Industrial Engineering (DIIN)
University of Salerno
Fisciano 84084, Italy
e-mail: rosantoriello@unisa.it, vcitro@unisa.it, web page: https://www.unisa.it

[†]Gran Sasso Science Institute (GSSI)
Viale F. Crispi 7, 67100 L'Aquila, Italy
e-mail: francesco.viola@gssi.it - Web page: https://www.gssi.it

Key words: multiphysics problems, swimmer, bio-hybrid, salp, cardiac muscle, pulse jet

Abstract. Biological systems can inspire the development of bio-hybrid swimmers, also called *biobots*, that integrate abiotic and biotic components into an engineered construct embedding life-like biomimetic behaviours and functions. Beyond bio-mimicry, biobots serve as platforms for testing new biological hypotheses, with the aim of extracting useful design principles. Here, we draw design inspiration from the locomotion and the simple cylindrical shape of salps to design a peristaltic swimmer, integrating cardiac muscle tissue for its functional capabilities with an artificial activation device. We investigate the performance of the biobot using a multiphysics numerical tool to determine the characteristics that influence the swimming dynamics. Our results indicate that optimal performance is achieved when a single wave propagates along the body and, as the contraction reaches the trailing edge, the peristaltic pattern begins again, avoiding inactivity phases and ensuring a continuous propulsion. Similar to salps, we observe an inverse relationship between the optimal actuation frequency and body length, suggesting that the same mechanism, *i.e.* the single wave propagation at a time, may govern the locomotion of salps as well. Overall, our findings provide new insights into the locomotion of salps and offer specific design principles that could be incorporated into the construction of bio-inspired and bio-hybrid robotic systems.

1 INTRODUCTION

Principles and mechanisms found in Nature have inspired scientists to develop bio-hybrid robots, also dubbed *biobots* [1, 2], by integrating artificial devices with biological elements, to build machines that can safely adapt to interact with the natural environment and also with humans [3]. The artificial part supplies the necessary actuation energy to the system, while the biological component (*e.g.*, the muscle tissue) provides the functional capabilities. Cardiac muscle tissue (the myocardium) has been a popular choice for the development of muscle-powered swimmers, since many forms of swimming involve continuous rhythmic movements [4]. Myocardium tissue, in fact, is composed of sheets of electrically coupled cells and is thus particularly suitable for constant and synchronous contractions that can be paced at different

frequencies. Inspiration from the body design of different marine organisms has generated a variety of biobots that mimic the forms and functional behaviours of these naturally existing systems. Examples are the *jellyfish-like* biobot developed by Nawroth *et al.* (2012) [5], made of chemically dissociated rat tissue and powered by external electrical stimulation; the *ray-like* biobot designed by Park *et al.* (2016) [6] made from rat heart muscle cells and actuated through optimal stimulation; and the *fish-like* biobot constructed by Lee *et al.* (2022) [7], powered by cardiac muscle tissue and equipped with an electrically autonomous pacing node to enhance spontaneous contractions. Integrating living cells into robotic systems can address many of the grand challenges in current robotics [8], such as reducing power consumption, improving damage tolerance, enabling adaptation to complex or unstructured environments, as well as allowing safe human-machine interaction. Beyond advancing robotics, biobots can also serve as a platform for testing new biological hypotheses [7], with the aim of extracting useful design principles [9]. Here, taking inspiration from the functioning of the human heart, as well as the locomotion and the simple geometry of salps, we propose the proof-of-concept of a peristaltic swimmer [10], integrating cardiac muscle tissue with an artificial activation device. The design of our biobot has been optimised using a multi-physics numerical tool that accounts for the hydrodynamics, the elastomechanics, and the electrophysiology, including their coupling, referred to as Fluid-Structure-Electro Interaction (FSEI) [11]. Our findings provide useful insights into the locomotion mechanism of salps, making the proposed proof-of-concept a valuable resource for guiding the design of future biohybrid systems.

The paper is organized as follows. First, in §2 we present the conceptual framework. Then, in §3 we provide a brief overview of the FSEI computational model. The following section (§4) is dedicated to the discussion of the numerical results. Concluding remarks are given in §5.

2 BIO-INSPIRED & BIO-HYBRID DESIGN

Salps are barrel-shaped marine invertebrates that swim via jet propulsion [12] (see the sketch in Fig.1*f*). They move forward by changing the volumes of their body cavity, drawing water into their muscular mantle cavity through the front aperture, and then expelling it under high pressure through the rear opening [13]. This process typically repeats at a frequency around $1\,Hz$ for forward swimming. If thought of as a chain of timed contractions, salp propulsion is reminiscent of peristaltic pumping applied to marine locomotion [14]. Given the remarkable adaptations of marine organisms in the underwater environment, it is natural to look to them for understanding how to move underwater (*bio-inspired biobot*). Then, the resulting bio-inspired prototype can serve as a platform to gain deeper understanding of the mechanism governing salp propulsion, with the aim of extracting useful design principles (*biobot unveils biology*) [15, 16].

Similar to salps, our biobot consists of a hollow cylinder that uses pulse-jet locomotion to propel itself through a fluid (see Fig.1*b*). Within the context of *bio-hybrid* design, the envisioned swimmer is made of working myocardium with fibres oriented in the the circumferential direction (analogous to salps that have circumferential muscle bands) to enable radial contraction, thereby facilitating peristaltic kinematics. Myocardium tissue has been chosen because of its contractile properties. It consists of cardio-myocytes, that are striated cells, electrically connected to one another through the so called "gap junctions" to form a functional syncytium [17] (a sketch of the myocardium tissue is shown in Fig.1*c*). Each myocyte depolarizes when it is reached by an electrical impulse and, in turn, it generates a new activation signal which is transmitted to neighbouring cells. At the microscopic level, this phenomenon is driven by
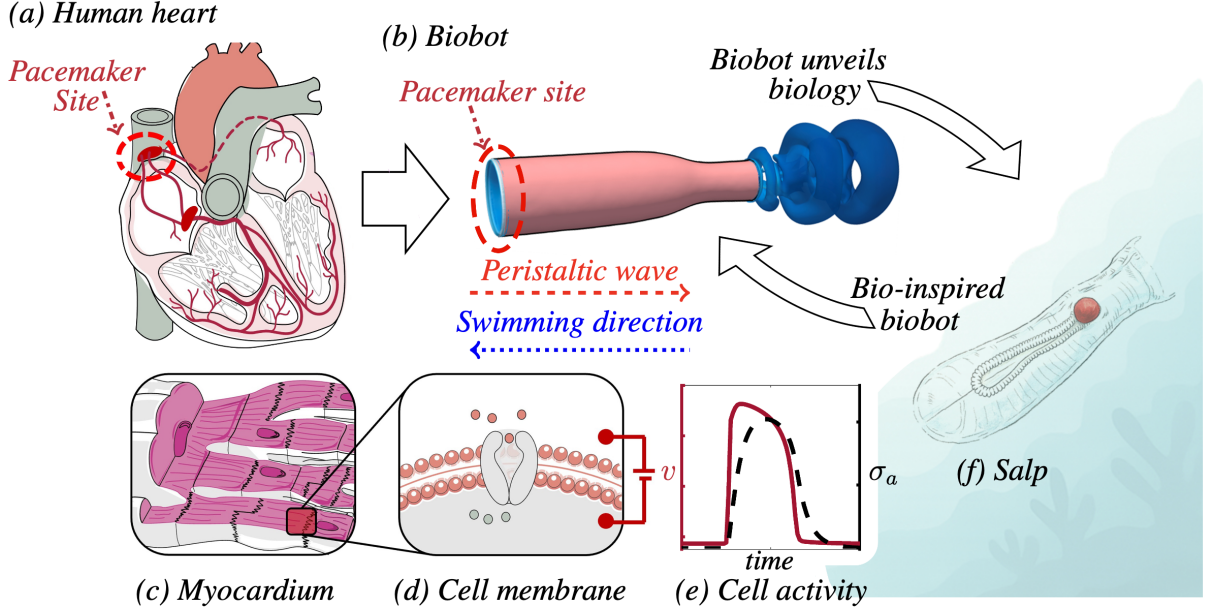
Figure 1: *(a)* Sketch of the human heart and its conduction system, including the primary pacemaker site; *(b)* proposed biobot, consisting of a circular cylinder made of cardiac muscle tissue and a pacemaker on the leading edge, which regulates the electric impulse; *(c)* sketch of the cardiac muscle tissue (the myocardium); *(d)* the cell membrane with an embedded protein; *(e)* relation between action potential (v) and active stress (σ_a) relative to a cell of the muscle tissue; *(f)* sketch of a salp.

the opening and closing of ionic channels, that are made of proteins located in the cell membrane (Fig.1*d*). The coordinated opening and closing of ionic channels sets the action potential (v ——), that consists in a rapid depolarization followed by a plateau and then a repolarization phase with the attainment of the initial negative potential (see the graph in Fig.1*e*). This transient depolarization produces an active tension (σ_a, see the dashed black line of Fig.1*e*) along the axis of the myocyte enabling its periodic contraction and relaxation. As in the human heart, some pacemaker cells triggers the synchronized contraction of muscle fibres to enable rhythmic blood pumping (Fig.1*a*), the driver of motion of our biobot is an electric current originating from a ring situated on the leading edge of the device that acts as a pacemaker, controlling the frequency of excitations (Fig.1*b*). The biobot is at rest in a quiescent fluid until the pacemaker activation initiates the propulsive cycle, triggering the muscular contractions throughout the cylindrical body. The synchronized contraction of cardiac cells results in a peristaltic wave, propagating from the leading edge to the trailing edge of the biobot. As the contraction propagates downstream, fluid is expelled out of the cylindrical body through an axisymmetric jet, whose evolution lead to the formation of a toroidal vortex. The resulting fluid instability [18, 19] provides the necessary thrust force to propel the swimmer in the opposite direction of the wave, thereby enabling forward locomotion.

3 METHODOLOGY

A Fluid–Structure-Electro Interaction (FSEI) numerical tool [20], based on an Immersed Boundary (IB) method [21] and a moving least squares (MLS) approach [22], has been adopted to design, simulate and optimize the swimming prototype through three-dimensional direct nu-

merical simulations (DNS). The fluid motion is obtained by directly solving the incompressible Navier-Stokes and continuity equations, which in non-dimensional form read as follows:

$$\frac{\partial \mathbf{u}}{\partial t} + \mathbf{u} \cdot \nabla \mathbf{u} = -\nabla p + \frac{1}{Re} \nabla^2 \mathbf{u} + \mathbf{f},$$

$$\nabla \cdot \mathbf{u} = 0, \tag{1}$$

where $\mathbf{u}$ and p indicate, respectively, the fluid velocity vector and pressure, while $\mathbf{f}$ represents the IB volume forcing required to impose the no–slip boundary condition at the fluid-structure interface. The Reynolds number is defined as $Re = UD/\nu$, where D denotes the diameter of the swimmer, U is a characteristic velocity common to all the swimmers investigated, and ν is the kinematic viscosity of the surrounding fluid. The Eqs.1 are numerically solved using the GPU version of the AFiD solver [23]. Details of the numerical scheme can be found in [24]. As detailed in [20], the output of the flow solver are the hydrodynamic loads ($\mathbf{F}_n^{ext}$) necessary to evolve the structural mechanics.

Moving on the electrophysiology subsystem, the propagation of the activation potential (v) through the myocardium is described by the monodomain equation coupled with a cell model:

$$\chi \left(C_m \frac{\partial v}{\partial t} + I_{ion}(\mathbf{s}) + I_s \right) = \nabla \cdot (\underline{\underline{\mathbf{M}}} \nabla v),$$

$$\frac{d\mathbf{s}}{dt} = F(\mathbf{s}, v, t), \tag{2}$$

where $\chi = 140 \ mm^{-1}$ and $C_m = 0.001 \ \mu F mm^{-2}$ denote the surface-to-volume ratio of cells and the membrane capacitance per unit area, respectively (set as in [25]), while $\underline{\underline{\mathbf{M}}}$ represents the conductivity tensor. The quantity $I_{ion}(\boldsymbol{s})$ is the ionic current per unit cell membrane, which is determined by the state vector $\boldsymbol{s}$ given by the cellular model [26] (the second equation of 2). Last, I_s is a prescribed input current which is necessary to initiate the electrical propagation through the myocardium tissue. The Eqs.2 are solved numerically as in Del Corso *et al.* (2022) [27], providing the distribution of the action potential at every instant. Then, using the relation suggested by Nash & Panfilov (2004) [28] the internal active tension (σ_n^{act}), at the nodes (n) of the computational grid of the structure, could be computed. The active tension translates into an active force according to $\mathbf{F}_n^{act} = \sigma_n^{act} S_n \hat{\mathbf{e}}_f$, where S_n is the local tissue cross section with respect to the fibre and $\hat{\mathbf{e}}_f$ is the local unit vector aligned along the fibres.

Finally, the structural dynamics is solved using a spring-network framework [22]. The swimmer is modelled as a triangulated surface and the mass is assumed to be equally distributed among the nodes of the triangles, that are connected by elastic springs, taking into accounts the energy due to the in-plane change of metric and the out-of-plane bending effects. The former if given by the elastic potential $W^e = 1/2 \ k_e x^2$, where k_e is the elastic constant [29] of a spring along the mesh edges, $x = l - l_0$ represents the edge deformation with l and l_0 being the spring length for the stretched and stress-free configuration, respectively. Taking the derivative of the potential energy with respect to displacements ($\mathbf{F}_n^{e,int} = \nabla W^e$), the nodal forces could be obtained. Considering a null reference curvature of the local surface, the bending elastic energy is given by $W^b = k_b(1 - \mathbf{n}_i \cdot \mathbf{n}_j) = k_b[1 - cos(\theta)]$, where $\mathbf{n}_i$ and $\mathbf{n}_j$ are the unit vectors normal to the triangular elements shared by the edge, θ is the angle between $\mathbf{n}_i$ and $\mathbf{n}_j$ and k_b is the bending constant, which is related to the averaged bending modulus B. Then, the nodal forces
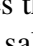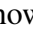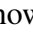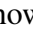
($\mathbf{F}_n^{b,int}$) corresponding to the bending energy could be obtained as in [22]. Consequently, we have the internal force as $\mathbf{F}_n^{int} = \mathbf{F}_n^{b,int} + \mathbf{F}_n^{e,int}$. To determine the instantaneous tissue configuration at each time step, for each node of the structure the second Newton law is integrated twice in time, considering the internal, external and the active forces,

$$m_n \ddot{\mathbf{x}}_n = \mathbf{F}_n^{ext} + \mathbf{F}_n^{int} + \mathbf{F}_n^{act}, \qquad (3)$$

where m_n is the mass of the node, while $\mathbf{x}_n$ is the instantaneous node position. The new geometry can then be used as input for the fluid and electrophysiology solvers to obtain the new active and external forces acting, in turn, on the tissue. Details of the algorithms and thorough validations can be found in the following references [11, 20, 27, 30].

4 RESULTS & DISCUSSION

A dimensional analysis of the governing equations reveals that the dynamics of the system is governed by two non-dimensional parameters. The first one is the Reynolds number Re (already introduced in §3), which quantifies the relative importance of inertial and viscous forces acting on the system. The second one is the Strouhal number $St = fD/U$, which corresponds to the non-dimensional actuation frequency f. All the results discussed in the following are presented in non-dimensional form.

To investigate the influence of design parameters (such as the actuation frequency and geometry) on swimming performance, we have monitored the mean value of the terminal swimming speed. The numerical results are reported in Fig.2a in terms of body length per second (L/s) versus Strouhal number, for all the configurations investigated, corresponding to swimmers with different body lengths $L = [2, 3, 4, 6]$, and a fix Reynolds number ($Re = 100$). All the curves exhibit a similar trend: the swimming speed increases almost linearly at low Strouhal numbers, reaches a peak, and then gradually decreases. It is evident that shorter biobots swim faster than their longer counterparts. Each curve (for a different value of L) is characterized by an optimal Strouhal number St_{opt} (highlighted with a red circular marker ⊙ in Fig.2a) that maximises the swimming speed and also the initial acceleration (the latter is not reported here for the sake of brevity). For the swimmer with $L = 2$, the peak of speed does not coincide exactly with that of the acceleration at $St = 1.667$, since a slightly higher value is recorded for a Strouhal number of $St = 1.5$ (specifically, $U(St = 1.5) = 2.40$ and $U(St = 1.667) = 2.36$). In the following, for the biobot with $L = 2$, the highlighted value for speed corresponds to the Strouhal numbers at which acceleration reaches its maximum value and speed is only slightly lower than the maximum value. A detailed investigation that takes into account also the initial acceleration will be presented in an extended version of the work. From this analysis (see Fig.2a) it is evident that the optimal Strouhal number is inherently related to the length of the biobot. Longer biobots require a lower Strouhal number to achieve optimal performance, while as the body length decreases, the Strouhal number required to reach the maximum speed increases. Indeed, for the longest ($L = 6$) and the shortest ($L = 2$) swimmers investigated, the optimal performance is recorded at $St_{opt} = 0.834$ and $St_{opt} = 1.667$, respectively. Focusing on a curve for a fix value of the body length (*e.g.*, $L = 4$), the body kinematics of the swimmer in the optimal case (corresponding to the red circular marker ⊙; in Fig.2a) and in some sub-optimal conditions (corresponding to the blue ⊙ ; and green ⊙ circular markers in Fig.2a) is shown in the sequence of snapshots of Figs.2b,c,d. We observe that the optimal scenario is achieved when a single contraction traverses the entire cylinder and, upon reaching the end of the body,

the peristaltic cycle immediately restarts (see Fig.2c). On the other hand, if the Strouhal number is lower than optimal value ($St < St_{opt}$), there are phases in the cycle where thrust is generated, followed by periods of inactivity before the next contraction occurs (see Fig.2b). Conversely, if the Strouhal number exceeds the optimal value ($St > St_{opt}$), multiple contractions propagate simultaneously, leading to destructive interferences (see Fig.2d). In the bottom panel of Fig.2 (see Figs.2e-h) we have reported the body kinematics and the vorticity fields for the optimal conditions of each body length investigated (highlighted in the graph of Fig.2a with red circular markers). A detailed examination of Figs.2e-h reveals that peak performance is achieved, when a single peristaltic wave propagates at a time along the body, regardless of the length of the swimmer. We highlight that the speed of the peristaltic wave is constant across all the configurations considered, as it is determined by the electrophysiological model. Consequently, to guarantee the propagation of a single wave at a time, longer swimmers require a lower excitation frequency because the peristaltic wave takes more time to travel through the elongated body. On the other hand, shorter swimmers require an higher actuation frequency due to the reduced length of their bodies.

The inverse relationship between the pulse frequency (represented here with the dimensionless Strouhal number St) and body length (L) is something observed in the locomotion of salps by Sutherland & Madin, (2010) [31]. According to their work (see Table 1 of their study), salp species with shorter body lengths, such as *Weelia cylindrica* (with mean length of $3.95\ cm$), exhibit higher pulse frequencies (corresponding to a Strouhal number of approximately $St \approx 2$, when rescaled according to our reference dimensions). On the other hand, longer salps such as *Pegea confederata* and *Cyclosalpa affinis* (with mean lengths of $5.08\ cm$ and $6.41\ cm$, respectively) show lower pulse frequencies, corresponding to Strouhal numbers of approximately $St \approx 1.5$ and $St \approx 0.8$. The same relationship between the pulse frequency and the body length was also observed by Harbison and Campenot (1979) [32] (see Fig.6 of their work). They reported that, at a constant temperature, the pulsation rate was inversely proportional to body length in all hand-collected salps. However, this relationship was not observed in trawl-collected salps, as the damage incurred during collection altered their natural behaviour. Consequently, they used this relationship to evaluate the collection methods and verify the physiological condition of the salps, thereby ensuring the validity of the experiment. In Fig.3, we report the regression curve obtained by Harbison and Campenot (1979) [32], illustrating the dependence of Strouhal number on body length for four species of *Salpa* (*i.e.*, *Salpa cylindrica*, *Salpa maxima*, *Salpa fusiformis*, and *Salpa aspera*) along with the 95% confidence limits. The same inverse relationship was also observed for Pegea confoederata (see Fig.3 of their study) and, as stated by the authors: *"this relationship probably holds for all salps"* [32]. We can observe that our findings (see Fig.3) follow a similar trend, as the optimal Strouhal number decreases linearly when moving from shorter swimmers ($L = 2$) to longer ones ($L = 6$). Also, as the optimal Strouhal number increases, the swimming speed increases as well (this is evident from the points highlighted with a red circular marker in Fig.2a). A similar trend was observed for salps, as reported by Madin (1990) [33]. Therefore, we can conclude that as the optimal Strouhal number increases, the optimal swimming speed of the biobot increases as well and this is accompanied by a decrease in body length. The alignment of our results with the experimental measurements on salps, suggests that the locomotion of salps is likely governed by the mechanism of a single wave propagation at a time. In the inertial regime, the simultaneous propagation of multiple contractions along the length of the swimmer leads to destructive
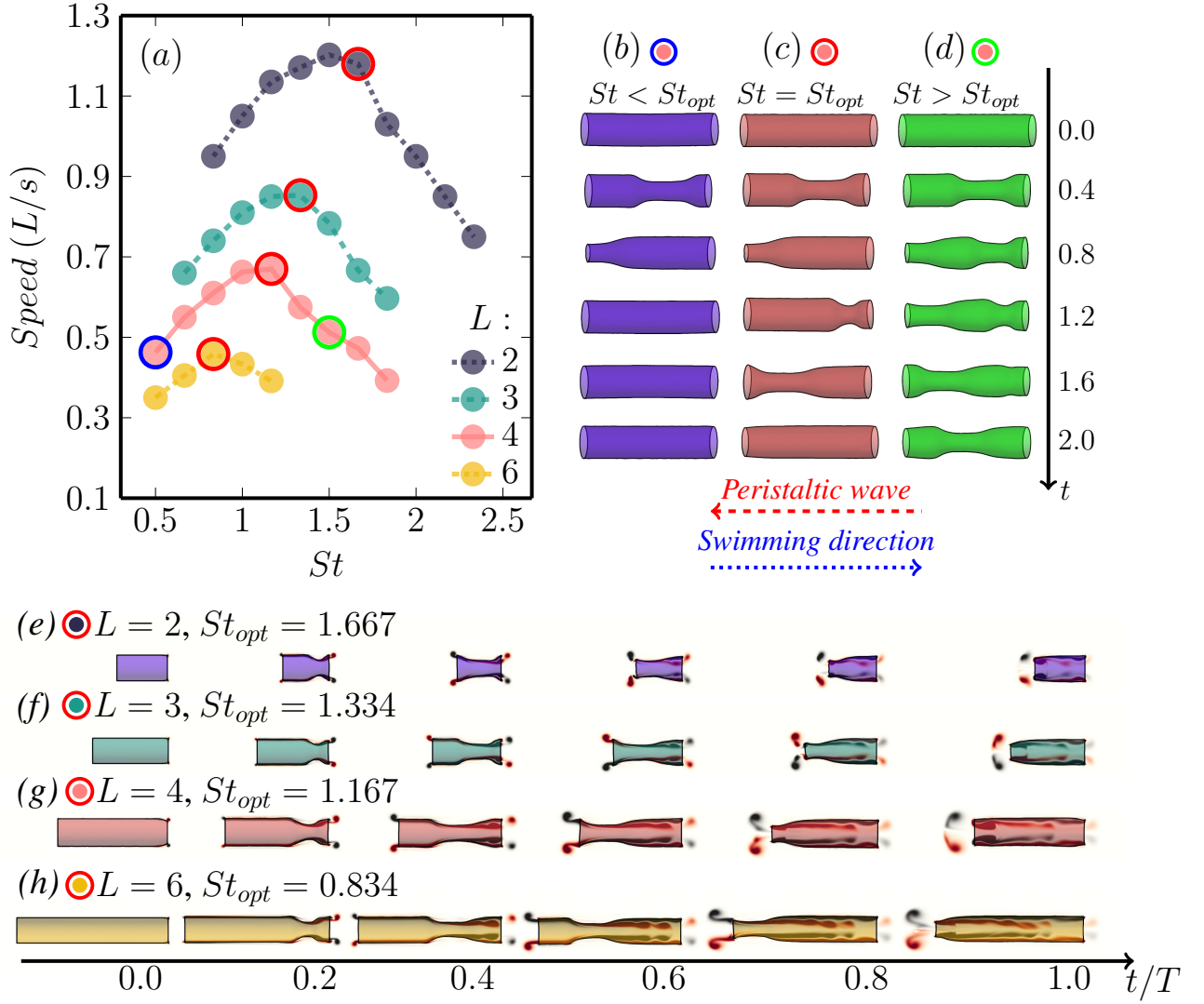
Figure 2: *(a)* Body length per seconds versus Strouhal number, parametrized by the body length (L) of the swimmers, for $Re = 100$. The red circular markers highlight the maximum values of swimming speeds. The swimmer's kinematics corresponding to the points highlighted in the graph (see the curve for $L = 4$) with blue, red and green markers, are shown on the right *(b,c,d)*. The dashed red arrow indicates the direction of the propagating peristaltic wave, while the dotted blue arrow indicates the swimming direction. The contour plots *(e–h)* illustrate the out-of-plane vorticity component (ω_x) fields during one period (T) of excitation, corresponding to the highlighted points in the graph with red circular markers. The vorticity field of all the plots is scaled from -20 (black) to 20 (red).

interferences. This phenomenon is not observed in the Stokes regime, where existing models suggest that an increase in the number of pulsations can enhance swimming speed [34]. In the present case, as the actuation frequency increases, the swimming speed exhibits a linear growth (see Fig.2*a*), which can be attributed to the partialization of thrust due to the inactivity phases between the pulses. However, beyond a threshold, where a single wave propagates per stimulation cycle and the peristaltic pattern restarts without inactivity phases, the speed reaches a maximum and then decreasing linearly as well, due to energy losses caused by the interference between multiple waves.
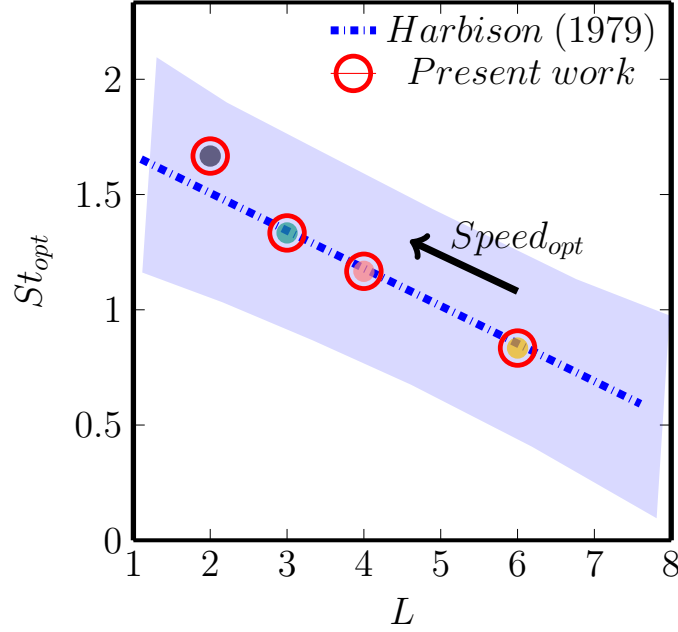
Figure 3: Relation between body length L and optimal Strouhal number St_{opt}. The dashed blue line shows the least-squares regression reported in Fig.6 of Harbison and Campenot (1974) [32]. The blue area represents the 95 % confidence limits associated with their data. The circular markers represent the results of the present study, showing the optimal Strouhal number identified for each tested body length. The black arrow represents the direction of optimal speed increase: it increases as the optimal Strouhal number increases as well, and the body length decreases (as indicated by the points highlighted with a red circular marker in Fig.2a).

5 CONCLUDING REMARKS

We presented the proof of concept of a peristaltic swimmer, integrating cardiac muscle tissue for its functional capabilities and an artificial activation device. The locomotion of our biobot results from the interconnected dynamics of (i) the electrophysiology system, responsible for the action potential propagation that triggers the active muscular tension, (ii) the internal passive forces of the biological tissue, and (iii) the hydrodynamic loads due to the interaction with the surrounding fluid. By simultaneously accounting for the Fluid-Structure-Electrophysiology Interaction (FSEI), our multi-physics computational tool allows us to predict and optimize the swimming dynamics through three-dimensional direct numerical simulations. The insights gained from the locomotion of our biobot, has led us to develop the hypothesis that the propagation of one peristaltic wave at a time, represents the key mechanism that causes salps to swim at a specific frequency. If the pulse frequency is too low, there will be periods of inactivity in the swimming cycle. On the other hand, the simultaneous propagation of multiple contractions leads to destructive interferences. Overall, our findings offer new insights into the locomotion of salps and suggest specific design features that could be incorporated into the construction of bio-inspired robotic vehicles.

Fig.1 was partially drawn using images from Servier Medical Art (https://smart.servier.com/), licensed under a Creative Commons Attribution 4.0 Unported License (CC BY).

REFERENCES

[1] Ricotti, L., et al. Biohybrid actuators for robotics: A review of devices actuated by living cells. *Science robotics*, (2017), **2.12:** eaaq0495.

[2] Kamm, R. D.; Bashir, R. Creating living cellular machines. *Annals of biomedical engineering*, (2014), **42.2:** 445-459.

[3] Raman, R.; Laschi, C. Soft robotics for human health. *Device*, (2024), **2.7.**

[4] Raman, R. Biofabrication of living actuators. *Annual Review of Biomedical Engineering*, (2024), **26.1:** 223-245.

[5] Nawroth, J.C., et al. A tissue-engineered jellyfish with biomimetic propulsion. *Nature biotechnology*, (2012), **30.8:** 792-797.

[6] Park, S.J., et al. Phototactic guidance of a tissue-engineered soft-robotic ray. *Science*, (2016), **353.6295:** 158-162.

[7] Lee, K.Y., et al. An autonomously swimming biohybrid fish designed with human cardiac biophysics. *Science*, (2022), **375.6581:** 639-647.

[8] Yang, G.Z., et al. The grand challenges of science robotics. *Science robotics*, (2018), **3.14:** eaar7650.

[9] Van Buren, T.; Floryan, D.; Smits, A. J. Bioinspired underwater propulsors. *Bioinspired structures and design*, (2020), 113-139.

[10] Santoriello, R., et al. Muscular tissue-driven swimming: a new BioBot. In: Abstract-AIMETA 2024 Naples. (2024). p. 1-1

[11] Viola, F.; Meschini, V.; Verzicco, R.. Fluid–structure-electrophysiology interaction (FSEI) in the left-heart: a multi-way coupled computational model. *European Journal of Mechanics-B/Fluids*, (2020), **79:** 212-232.

[12] Costello, J. H., et al. The hydrodynamics of jellyfish swimming. *Annual Review of Marine Science*, (2021), **13.1:** 375-396.

[13] Madin, L P. FIELD STUDIES ON THE BIOLOGY OF SALPS (TUNICATA: THALIACEA). University of California, Davis, 1974.

[14] Athanassiadis, A.; Hart, D. Hydrodynamics of Peristaltic Propulsion. In: *APS Division of Fluid Dynamics Meeting Abstracts.* (2014). p. L12. 001.

[15] Lauder, G. V.; Madden, P. GA. Learning from fish: kinematics and experimental hydrodynamics for roboticists. *International journal of automation and computing*, 2006, **3.4:** 325-335.

[16] Gravish, N; Lauder, G. V. Robotics-inspired biology. *Journal of Experimental Biology*, (2018), **221.7:** jeb138438.

[17] Katz, A. M. Physiology of the Heart. *Lippincott Williams & Wilkins*, (2010).

[18] Citro, V., et al. A sensitivity-based protocol for identifying non-viscous mechanisms causing fluid dynamic instabilities. In: Abstract-AIMETA 2024 Naples. (2024). p. 1-1

[19] Santoriello, R., et al. Characterisation of the secondary instability in a 1:3 sudden expansion through inviscid structural sensitivity. *Submitted to Journal of Fluid Mechanics*.

[20] Viola, F., et al. GPU accelerated digital twins of the human heart open new routes for cardiovascular research. *Scientific reports* (2023) **13.1**: 8230.

[21] Verzicco, R. Immersed boundary methods: Historical perspective and future outlook. *Annual Review of Fluid Mechanics*, 2023, **55.1:** 129-155.

[22] de Tullio, M.D.; Pascazio, G. A moving-least-squares immersed boundary method for simulating the fluid–structure interaction of elastic bodies with arbitrary thickness. *Journal of Computational Physics*, (2016), **325:** 201-225.

[23] Viola, F., et al. AFiD-GPU: A versatile Navier–Stokes solver for wall-bounded turbulent flows on GPU clusters. *Computer physics communications*, (2018), **229:** 199-210.

[24] Verzicco, R; Orlandi, P. A finite-difference scheme for three-dimensional incompressible flows in cylindrical coordinates. *Journal of Computational Physics*, 1996, **123.2:** 402-414.

[25] Niedered, S. A., et al. Verification of cardiac tissue electrophysiology simulators using an N-version benchmark. *Philosophical Transactions of the Royal Society A: Mathematical, Physical and Engineering Sciences*, 2011, **369.1954:** 4331-4351.

[26] Ten Tusscher, K. HWJ; Panfilov, A. V. Cell model for efficient simulation of wave propagation in human ventricular tissue under normal and pathological conditions. *Physics in Medicine & Biology*, 2006, **51.23:** 6141.

[27] Del Corso, G.; Verzicco, R.; Viola, F. A fast computational model for the electrophysiology of the whole human heart. *Journal of computational physics*, (2022), **457:** 111084.

[28] Nash, M. P.; Panfilov, A. V. Electromechanical model of excitable tissue to study reentrant cardiac arrhythmias. *Progress in biophysics and molecular biology*, 2004, **85.2-3:** 501-522.

[29] Gelder, A. V. Approximate simulation of elastic membranes by triangulated spring meshes. *Journal of graphics tools*, 1998, **3.2:** 21-41.

[30] Viola, F., et al. FSEI-GPU: GPU accelerated simulations of the fluid–structure–electrophysiology interaction in the left heart. *Computer physics communications*, (2022), **273:** 108248.

[31] Sutherland, K. R.; Madin, L. P. Comparative jet wake structure and swimming performance of salps. *Journal of Experimental Biology*, (2010), **213.17:** 2967-2975.

[32] Harbison, G. R.; Campenot, R. B. Effects of temperature on the swimming of salps (Tunicata, Thaliacea): Implications for vertical migration 1. *Limnology and Oceanography*, (1979), **24.6:** 1081-1091.

[33] Madin, L. P. Aspects of jet propulsion in salps. *Canadian Journal of Zoology*, (1990), **68.4:** 765-777.

[34] Ajdari, A.; Stone, H. A. A note on swimming using internally generated traveling waves. *Physics of Fluids*, (1999), **11.5:** 1275-1277.

[35] Zienkiewicz, O.C. and Taylor, R.L. *The finite element method*. McGraw Hill, Vol. I., (1989), Vol. II., (1991).

[36] Idelsohn, S.R. and Oñate, E. Finite element and finite volumes. Two good friends. *Int. J. Num. Meth. Engng.* (1994) **37**:3323–3341.